TITLE: Detection of maturity and ligament injury using magic angle directional imaging

AUTHORS: Karyn E. Chappell, Djordje Brujic, Catherine Van Der Straeten, Richard Meeson, Wladyslaw Gedroyc, Donald McRobbie, Mihailo Ristic

JOURNAL: Magnetic Resonance in Medicine

PUBLISHER: Wiley

PUBLICATION DATE: 12 May 2019 (online)

DOI: https://doi.org/10.1002/mrm.27794

Detection of Maturity and Ligament Injury Using Magic Angle Directional Imaging (MADI)

Karyn E Chappell[1], Djordje Brujic[3], Catherine Van Der Straeten[1], Richard Meeson[2], Wladyslaw Gedroyc[4], Donald McRobbie[1], Mihailo Ristic[3]
[1] Imperial College London, Department of Surgery and Cancer, MSK Lab, UK;
[2] Royal Veterinary College, Department of Clinical Sciences and Services, Hertfordshire, UK
[3] Imperial College London, Department of Mechanical Engineering, UK;
[4] Imperial College Healthcare NHS Trust, St Mary's Hospital, MRI Unit, UK;

Corresponding author: Mihailo Ristic, Imperial College London, Mechanical Engineering Department, South Kensington Campus, London SW7 2AZ, United Kingdom, Tel: +44 20 7594 7048, m.ristic@imperial.ac.uk

ABSTRACT

Purpose: To investigate whether magnetic field related anisotropies of collagen may be correlated with post mortem findings in animal models.

Methods: Optimised scan planning and new MRI data processing methods were proposed and analysed using Monte Carlo simulations. Six caprine and ten canine knees were scanned at various orientations to the main magnetic field. Image intensities in segmented voxels were used to compute the orientation vectors of the collagen fibres. Vector field and tractography plots were computed. Alignment Index (AI) was defined as a measure of orientation distribution. The knees were subsequently assessed by a specialist orthopaedic veterinarian who gave a pathological diagnosis having dissected and photographed the joints.

Results: Using 50% less scans than reported previously can lead to robust calculation of fibre orientations in the presence of noise, with much higher accuracy. The six caprine knees were found to range from very immature (<3 months) to very mature (>3 years). Mature specimens exhibited significantly more aligned collagen fibres in their patella tendons compared to the immature ones. In two of the ten canine knees scanned, partial cranial caudal ligament (CCL) tears were identified from MRI and subsequently confirmed, with encouragingly high consistency of tractography, AI and dissection results.

Conclusion: The method can be used to detect injury such as partial ligament tears, and to visualise maturity related changes in the collagen structure of tendons. It can provide the basis for new non-invasive diagnostic tools in combination with new scanner configurations that allow less restricted field orientations.

Keywords: magic angle effect, collagen, musculoskeletal imaging

Word count: 6146

1. INTRODUCTION

Conventional MRI and other non-invasive soft tissue imaging modalities do not provide sufficient information for accurate diagnosis of injury or disease in ligaments, tendons, menisci, and also in articular cartilage, and muscle fibres. Such tissues contain significant amounts of collagen arranged in fibre structures, in which the dipolar coupling is a very significant signal decay mechanism, resulting in a very short transverse relaxation time T_2. Consequently these tissues normally appear black (having no observed signal) and any bright regions are possible artefacts, or possible signs of disease or injury. It is mainly due to this phenomenon that the diagnosis of conditions in joints remains a challenge. Invasive methods such as arthroscopy or open surgery remain as the generally accepted diagnostic gold standard, even though they are normally undertaken only as treatment [1-3].

The dependence of the strength of dipolar interactions on the orientation of the magnetic field in collagen bound water molecules was first observed by Berendsen [4] when studying NMR spectra of partially hydrated collagen. Fullerton *et al* [5] observed the same effect in bovine tendons at physiological hydration levels and its effect on the transverse relaxation time T_2/T_2^*. Erickson *et al* [6] reported significant changes in image intensity due to magic angle effect in certain tissues during routine MRI examinations, and showed that they are most pronounced in sequences with short echo time TE [7].

The strength of the residual dipolar interactions depends on the angle θ between the proton-proton direction and the direction of the magnetic field, and it is modulated by the term $(3cos^2\theta - 1)$, which will diminish when $\theta = 54.7°$, commonly known as the magic angle. The observed signal intensity in MRI images may be considered to involve contributions from two proton species, one corresponding to the water molecules bound to collagen, forming a chain structure and exhibiting an anisotropic field-angle dependent $T_{2,a}^*$, and the other corresponding to unrestricted water molecules in gaps and exhibiting an isotropic $T_{2,i}^*$ [8,9]. The reported T_2 values measured for tissues such tendons, ligaments and cartilage [7,8,10] showed field angle dependent variations in the range from about 1 ms to about 25 ms. Consequently, imaging sequences with short TE (e.g.TE<37 ms) show a marked intensity variation due to the magic angle effect.

While this effect is usually seen as a source of artefacts, Szeverenyi and Bydder [9] have shown that it is possible to deduce the dominant collagen fibre orientation in each voxel by imaging the subject at various orientations to the main field and by analysing the resulting image intensity variation. In their work they analysed an excised goat meniscus and were able to generate tractography plots depicting the underlying collagen structures. Siedel *et al*. [11] employed a similar approach to analyse an excised human iliotibial band and verified the results using polarised microscopy. In this exploratory research there was little attempt to optimise the number of required orientations relative to B_0, so in [11] the sample was scanned at 37 orientations, while in [9] 15 orientations were used.

The work presented in this paper has been motivated by our continuing development of a novel transverse field MRI scanner [12], which has been designed to enable imaging of this type to be performed in the future *in-vivo* on human subjects. It employs a unique magnet configuration in which the net field is parallel to the poles. The magnet is mounted on a 2 degree-of freedom motorised structure to allow a wide range of angulations to be achieved. The Magic Angle Directional Imaging method presented below was designed to be compatible with this system.

Our hypothesis is that the results of Magic Angle Directional Imaging can be correlated with the findings of post mortem dissection, so that it can serve as a basis for future diagnostic methods. Our objective was also to investigate how the number of the required scanning orientations of the subject relative to B_0 may be optimised in a general case and in the presence of noise, in order to reduce the scanning time. Furthermore, we propose improved methods for the processing of angle sensitive MRI data that lead to significantly improved computing speed and accuracy.

2. METHODS

2.1 Imaging and Image Processing

2.1.1 The Overall MR Imaging and Image Processing Pipeline

The imaging and image processing pipeline is presented below and the main computational outputs are illustrated in Figure 1. All software was developed in Matlab (Mathworks, Inc.), except for tractography visualization which was performed using ParaView (Sandia National Laboratory). The steps in the overall process are as follows.

1. Multiple MR volume images are obtained at N equispaced 3D orientations of the subject relative to B_0. The orientations are equispaced if the minimum angle between them is a maximum. In this work the specimen was mounted in a suitable support structure and it was rotated to a new orientation for each new MRI acquisition. We adopted typical isotropic voxel size of 1mm.
2. The acquired volume images are registered in order to establish voxel correspondences.
3. Variation of signal intensity for each voxel is analysed to identify the regions showing any significant dependence on the angle of B_0. Segmentation of those regions is performed in order to substantially reduce the dataset required for the subsequent processing and to speed up the computations. Interactive user tools were also provided in order to control the region of interest.
4. Nelder-Mead simplex algorithm was used to estimate the dominant fibre orientation in each segmented voxel from the set of measured intensities. The result of the process are the calculated fibre direction vectors for each voxel. Such data may be displayed in 3D using glyphs (a form of a vector field plot), but for better visualisation it may be used to generate 3D tractography plots.
5. Finally, relevant metrics may be calculated for the region of interest, such as the distribution of collagen fibre orientations and the alignment index (Sec 2.1.6)

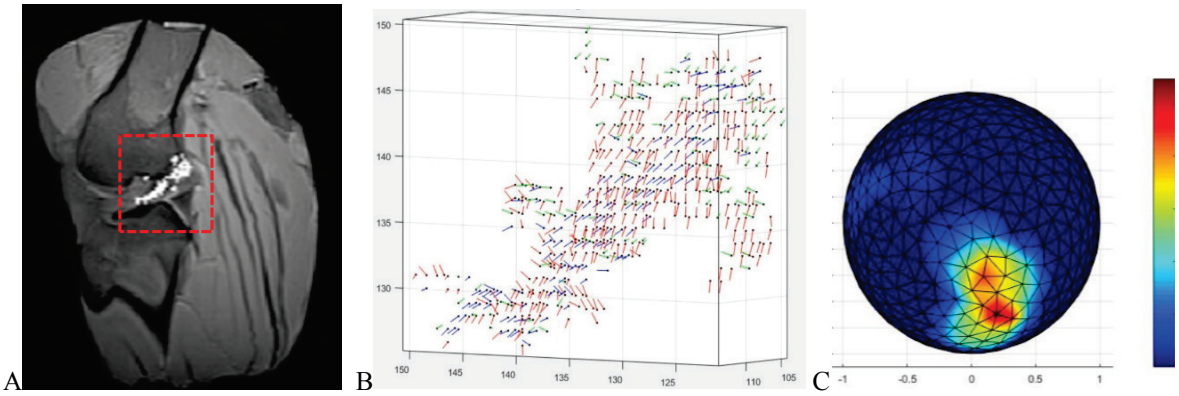

FIGURE 1 Data processing steps following registration of image volumes acquired at different orientations to the field B_0. **A**: Region of interest is interactively selected, voxels within it with intensity variations exceeding a threshold are highlighted as white, and segmented. **B**: Dominant fibre orientations in each voxel are determined and displayed as a 3D vector field. **C**: 3D polar plot of the frequency distribution of fibre orientations in the segmented voxels.

2.1.2 Registration

In principle the images may be aligned by rotating each volume according to the *a priori* defined scanning orientations, but in practice it may be difficult to control the rotation to a high accuracy, nor to measure the applied rotation accurately.

Registration was performed using passive markers, consisting of three or more water filled balls with a diameter of 10mm which were rigidly held with the sample. Localization of the markers in the images was performed using the template matching method, which relies on their spherical shape. Similarly to [13] the Fourier Filtering Method [14] is employed, however, here it is applied to a volume instead of 2D images. Previous work [15] indicated that the typical accuracy of the localization method is better than 0.3 voxels. If the markers are arranged in a known pattern such that they are not equidistant from each other, then the correspondence between identified marker positions in different volume images can be established automatically [16]. Registration is then performed as a rigid body transformation that minimizes the sum of the squared distances between the corresponding marker points [17]. In the final step, nearest neighbour method is used to establish voxel-voxel correspondences between all acquired volumes.

In the presence of image distortions, caused primarily by the non-linearities of the gradients and non-uniformity of the main field, it was often found necessary to perform manual fine alignment of images, typically applying translations of about one voxel, in order to improve the alignment accuracy in the central region of interest.

2.1.3 Segmentation

Having found the corresponding voxels, a map of signal intensity variation is computed. The normalized standard deviation of a voxel's intensity obtained for all orientations was taken as a measure of the size of the residual dipolar coupling, representing the coefficient of variation [9]. Voxels with intensity variation exceeding a predefined threshold are highlighted (Figure 1A). A specific volume of interest may be selected interactively by a user-defined bounding box and segmented out, significantly reducing the dataset required for processing and speeding up the computations.

2.1.4 Computation of Fibre Orientations

The segmented voxels are assumed to contain oriented collagen and have a vector of N intensities $\boldsymbol{I}_m$ that correspond to known directions of the field B_0 relative to the specimen (scanning direction). As proposed in [9] the dependence of image intensity I on the field angle θ may be modelled using the relationship

$$I = A\, exp(-B(3\cos^2\theta - 1)^2) \qquad (1)$$

where the constants A and B are chosen such that the range of corresponding values of I matches the observed range of intensities in the acquired images.

For calculation of the fibre orientations we construct the cost function

$$f(\boldsymbol{\Phi}) = \sum_{k=1}^{N} \left(\boldsymbol{I}_m(k) - \boldsymbol{I}_c(\boldsymbol{\Phi}, k)\right)^2 \qquad (2)$$

where $\boldsymbol{I}_m(k)$ represents intensity of a voxel scanned in the k-th direction, $\boldsymbol{I}_c(\boldsymbol{\Phi}, k)$ represents the computed theoretical intensity that a fibre with direction $\boldsymbol{\Phi}$ would have if it was scanned in the k-th scanning direction. The direction $\boldsymbol{\Phi} = (\phi, \psi)$ is defined in the spherical coordinate system and the minimisation of $f(\boldsymbol{\Phi})$ involves 2 dimensions. The cost function is highly non-linear and the Nelder-Mead simplex algorithm [18] was used for minimisation as it does not require computation of derivatives.

The algorithm first makes a simplex of 3 points around the initial guess $\boldsymbol{\Phi}_0$. In order to find the initial guess for the iterative search, we have computed theoretical intensities $\boldsymbol{I}_c$ for M template directions using Equation (1), which are regularly distributed on a hemisphere. The direction with the highest correlation to the measured intensities $\boldsymbol{I}_m$ for a given voxel was accepted as the initial guess $\boldsymbol{\Phi}_0$. The search for the initial guess is similar to the method suggested by Szeverenyi

[9] with the main difference that the orientation which they take as a final result is only the initial guess for our minimisation. Also, we compute the correlation coefficient by its formal definition, not as a dot vector product of intensities.

The minimization of Equation (2) has multiple minima due to the angular symmetry of image intensity and it is also influenced by the image noise, so the achievement of the correct minimum crucially depends on a sufficiently accurate initial guess. The analysis of the required number of equispaced test directions that lead to a sufficiently good initial guess in the presence of noise was performed using Monte Carlo Simulations as described in Sec. 2.2, and the results are presented in Sec. 3.1.2. The test directions were generated for a hemisphere from an initial equal area partitioning of a unit sphere [19].

2.1.5 Visualisation of Collagen Tracts

The 3D vector field data of fibre orientations (Figure 1B) was further processed using ParaView software (Sandia National Labs), allowing both glyph plots (vector field) and 3D tractography plots using streamlines. The choice of visualization method may be a matter of user preference, however we found glyph plots to be more informative in the case of articular cartilage and menisci, while streamlines were found to be preferable in the case of ligaments and tendons. In all cases red-green-blue colour coding of directions corresponding to x-y-z axes was found to improve visualisation.

2.1.6 Orientation distribution and Alignment Index (AI)

For a computed vector field of fibre orientations, it is useful to visualise and to quantify the distribution of those orientations in order to facilitate a better understanding of the tissue anisotropy. The fibre orientations may be described by a spatial density distribution which quantifies the volumetric fraction of fibres oriented in a particular direction. As a suitable metric describing the degree of orientation anisotropy we propose the use of the Alignment Index (AI). AI identifies the fraction of voxels in the segmented set that have dominant fibre orientations aligned within 20° solid angle of the peak orientation, and this is normalised to the fraction of randomly oriented fibres that would lie within this range. This was implemented as follows.

The calculated set of fibre orientations, each associated with a corresponding segmented voxel, can be represented by a polar plot of unit vectors. For these, the spatial density distribution is computed using a frequency based approach involving regular bins. Since the traditional method of constructing bins on a sphere via lines of latitude and longitude results in variable sized facets, we again employed Leopardi's algorithm [19] that provides a method for tessellation of the sphere into regions of equal areas and results in triangular facets. Then, for each vertex in this tessellation we find the number of orientations in the data set that are closer to it than to any other vertex. The distribution density calculated for each vertex is coded in colour and the overall results is illustrated in Figure 1C. From this, the locations and magnitudes of peaks in the density distribution can be readily identified.

The AI may be calculated for any chosen orientation, but it is clearly most useful for the one corresponding to the distribution peak. For tissue regions in which more than one dominant direction can be observed, calculating an AI for each could be more appropriate. AI was calculated using the following equations:

$$\begin{aligned} &\text{if } n_M \geq n_{Rnd} \quad \text{then} \quad AI = \frac{(n_M - n_{Rnd})}{(n_{Total} - n_{Rnd})} \\ &\text{if } n_M < n_{Rnd} \quad \text{then} \quad AI = 0 \end{aligned} \tag{3}$$

where n_{Total} is the number of fibre orientations considered (i.e. the number of segmented voxels), n_M is the number of fibre orientations within the 20° solid angle relative to the chosen direction, and n_{Rnd} is the number or random orientations that falls within the same solid angle if n_{Total} random orientations are generated.

Accordingly, AI=0 indicates a fully isotropic vector set, and increasing AI values indicate increasingly aligned vector sets. AI=1 Indicates that all vectors are orientated within the 20° solid angle from the selected direction (i.e. the dominant alignment direction). For tissue regions in which more than one dominant direction can be observed, calculating an AI for each could be appropriate.

2.2 Simulation studies

The number of required volume image acquisitions at various orientations relative to B_0 is of great practical importance, bearing in mind that the scanning time may be significantly reduced by minimising the required number of such acquisitions. In their prior work Szeverenyi *et al* [9] performed volume acquisitions at 15 different orientations, which were confined to 3 orthogonal planes in 30° increments, while Siedel *et al* [11] used 37 orientations, confined to 2 orthogonal planes in 10° increments.

We postulated that maximum angle sensitive information could be extracted if the selected orientations are equispaced in 3D, meaning that the selected orientation vectors are not confined to specific planes, as illustrated in Figure 2 for 9 directions. No prior knowledge about the expected fibre orientation was assumed. Simulation studies were conducted in order to establish the required number of such orientations in the presence of image noise.

The sets of N equidistant scanning orientations were defined using the method for partitioning of the unit sphere into regions of equal area and small diameter [19] and recording the points at the centre of each region. The points corresponding to one hemisphere were then selected to define the direction vectors.

Monte Carlo simulation studies were conducted in order to investigate the robustness of the method in relation to the number of image acquisition orientations, and its accuracy of estimating fibre orientations. As the influence of noise can be a significant factor, both aspects were investigated for different SNR values.

Cases involving sets of between 5 and 13 scanning orientations were considered. Simulations in each case involved 10^5 trials in which a single voxel was considered and fibre orientation was randomly chosen. Angle dependent signal intensity was determined using Eq.1 with constants A=3000 and B=0.4 providing the best fit to the experimentally observed range of intensities. Randomly calculated noise was added to these theoretical values corresponding to various SNR values. The simulated intensity values were used in each case to estimate the fibre orientation.

2.3 MRI Experiments

All MRI experiments were performed with a 3T scanner (Magnetom Verio, Siemens, Erlangen, Germany) running Syngo Numaris B17. Permission to scan the animal knees was granted by the Hospital's Imaging Committee. A 12 channel head coil was selected to act as the signal receiver. Knees were scanned with a 3D T1 FLASH (Fast Low Angle Shot) sequence with 1mm isotropic voxels (TR13ms, TE4.9ms, FOV256mm, BW230Hz). The test sphere containing the knee was scanned in 9 directions to the main field B_0, which were set using suitable markings on the surface of the test sphere.

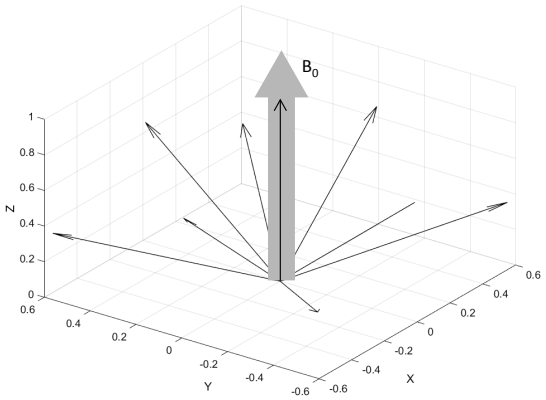

FIGURE 2 9 equidistant orientation vectors relative to B_0 in which the samples were scanned: (0, 0, 1), (0.661, 0, 0.75), (0, 0.661, 0.75), (-0.661, 0, 0.75), (0, -0.661, 0.75), (0.65, 0.65, 0.4), (-0.65, 0.65, 0.4), (-0.65, -0.65, 0.4), (0.65, -0.65, 0.4).

2.3.1 Specimen Collection and Preparation

Caprine specimens: Six caprine legs were purchased from a local meat supplier (W Wells Butchers Ltd) who could ensure that the goat had been slaughtered and then refrigerated at 4˚C for no more than five days. The caprine leg was shortened by the butcher using a saw and blade to 175mm with the joint line centralised at around 87mm (Figure 3A).

Canine specimens: Ethical approval was granted by the Royal Veterinary College London (URN 2017 1659-3) to collect knees from ten dogs who had been euthanized and required a post mortem (PM). The canine legs were removed during the initial PM by a technician and shortened to 180mm with the joint line centralised at 90mm. Knees were sealed in zip lock bags then refrigerated at 4˚C for no more than five days before scanning.

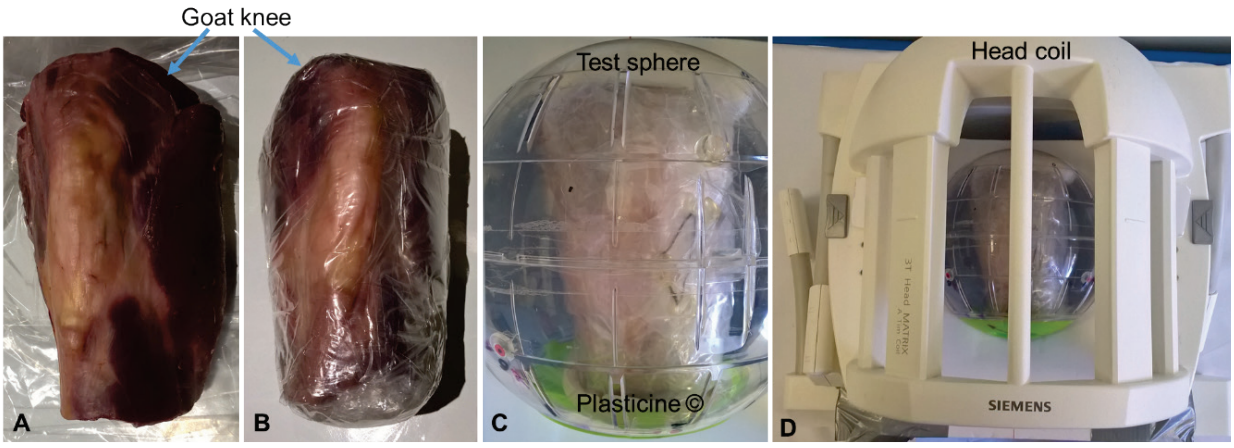

FIGURE 3 **A:** Goat knee after it had been cut down to 175mm and thoroughly cleaned of metal debris. **B**: Knee wrapped in polythene to prevent leakages and maintain tissue hydration covered in clear parcel tape to immobilise knee in extension. **C:** Goat knee within the test sphere with the proximal and distal ends embedded in white Plasticine. **D**: Test sphere containing goat knee within the 12 channel head coil in specially designed holder ready to begin scanning in position 1.

2.3.2 Specimen Mounting

The ends of the leg that had been cut were cleaned thoroughly in running water to remove any metal debris from the blade and saw which could cause susceptibility artefacts on the MRI images. The knee was wrapped in polythene to prevent leakages and to maintain tissue hydration (Figure 3B). To prevent the knee flexing and returning to its neutral position during the scan clear parcel tape was used to immobilise the leg in an extended position (clear polypropylene tape, 41µm x 48mm x 66m). Tape was applied to the proximal end pulled tight along the anterior aspect and fixed at the distal portion. Additional clear tape was applied to stabilise the quadriceps, hamstring muscles and other soft tissues. The knees were mounted inside the test sphere by embedding the distal and proximal ends in Plasticine (Figure 3C), which was selected as the embedding medium because it had no MRI signal in the tests performed by the researcher. This ensured that there was no movement of the knees within the sphere whilst the sphere was rotated in the holder fixed inside the 12 channel head coil (Figure 3D). The knee within the test sphere was centralised in the holder inside the scanner and positioned with the first scanning position aligned with the inferior red tick mark. Three water filled balls with a diameter of 10mm (.43 Caliber Clear Paintballs 8000, Rap4 UK) in a triangular alignment were fixed to the surface of the knee and one ball was on the inside of the test sphere.

2.4 Specimen investigation post scan

For the caprine samples, the unprocessed 3D T1 FLASH volume images were assessed by a specialist veterinary radiologist who estimated the ages of the animals based on the signal intensity of the bone marrow and the epiphyseal plates. Note that all animals were initially expected to have been slaughtered between 12-18 months and male, as they are a by-product of the goat diary industry. However, estimates suggest that three of the goats were less than 12 months and two were more than 3 years.

For the canine samples, following image data collection the samples were assessed by a specialist orthopaedic veterinarian who gave a pathological diagnosis having dissected and photographed the joint. These findings were later compared with the MR findings once the images were processed to determine if there is any correlation.

3. RESULTS

3.1 Simulation Studies

3.1.1 Required Number of Scanning Orientations

Monte Carlo simulations were conducted involving simulated image noise values of $SNR = 5, 10, 20, 40, 80$ and 1000, and the numbers of scanning orientations $N = 5, 7, 9, 13$, using 10^5 simulation runs in each case. The initial guesses for the simplex minimisations were found using 250 test directions (see 3.1.2 below). In each case we recorded the number of simulations that failed to converge correctly, which was judged by the error in calculating the orientation being $> 5°$. The results are summarised in Figure 4, showing the number of failed calculations as a function of SNR, for different values of N.

The overall aim was to achieve 99% success rate in calculating fibre orientations. The results show that for $SNR \geq 10$ this can be achieved with $N = 9$ scanning directions. For $SNR = 20$, $N = 7$ scanning directions are sufficient to achieve of 99.88% success rate, while $N = 5$ gives 98.5% success rate.

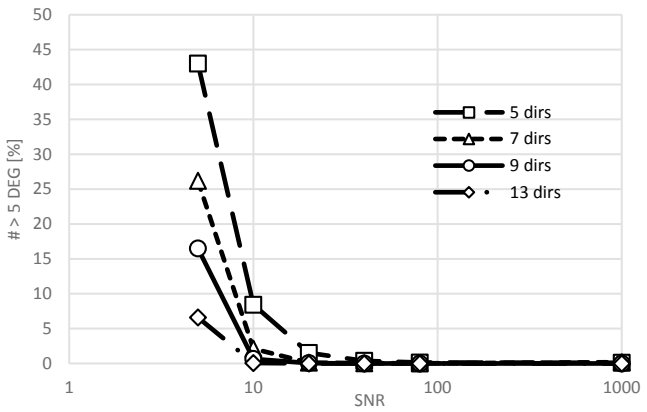

FIGURE 4 Monte Carlo simulation results showing number of failed (error> 5°) fibre orientation calculations in 10^5 simulations as a function of image SNR, for different numbers of equidistant scanning orientations relative to B_0.

3.1.2 Accuracy of Fibre Orientation Estimation

Based on the above results the number of scanning orientations was set to $N = 9$, considering the anticipated range of Signat-to-Noise Ratio (SNR) values and the desired robustness of calculation. The proposed simplex method for estimating fibre orientations requires an initial guess, obtained by examining a predefined number of test directions using the method in [9]. The required quality of the initial guess and therefore robustness in finding the global minimum was found to depend on the image SNR. Increasing the number of test directions improves robustness at the expense of a longer computing time.

Following extensive experimentation with different numbers of test directions and different noise values, it was concluded that for a coarse initial guess (e.g. 100 test directions, 16° angular resolution) there would be a small number of cases when convergence is not achieved, which resulted from only about 0.5% of the trial runs not converging. The robustness is improved significantly with the number of test directions above a threshold of about 200. The number of test directions was therefore set to 250 ($\approx 15°$ angular resolution) in all subsequent work to guarantee convergence.

The dependence of the error in estimating orientations w.r.t. SNR value was analysed and the results are shown in Figure 5, giving average, StDev and maximum angular error obtained through 10^3 Monte Carlo simulations each time. The small values of both average and StDev for low SNR values indicates that the algorithm failed to converge to a global minimum only in a few trials (less than 5 in 1000, i.e. <0.5%).

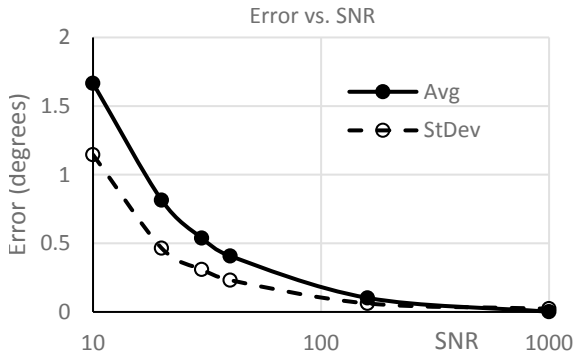

FIGURE 5 Average and standard deviation of error in estimating fibre directions as a function of SNR, using 250 test directions to find the initial guess for simplex minimisation. Each point involves 10^3 Monte Carlo simulations.

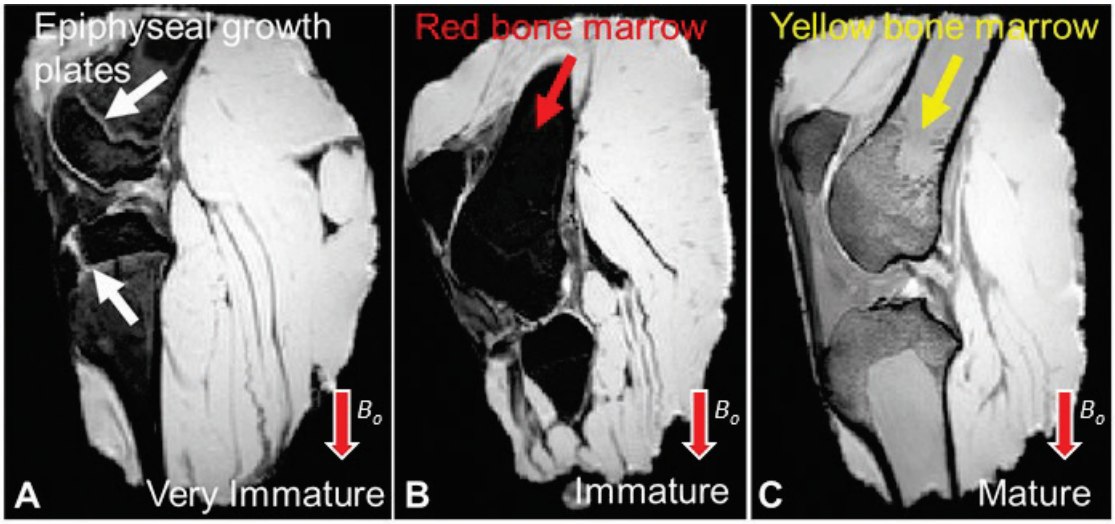

FIGURE 6 3D T1 FLASH central slice from three of the six specimens scanned showing the variation in the signal intensity of the immature (**A** and **B)** and mature (**C**) bone marrow. The femoral and tibial epiphyseal growth plates are unfused in the very immature (**A**) specimen which also has a similar signal intensity to the immature (**B**) specimens.

3.2 Experimental Studies

3.2.1 Caprine Knee Samples

The age of the caprine samples was initially expected to be similar for all samples and in the range of 12-18 months. However the MRI studies revealed that the samples varied in age significantly and ranged from very immature to very mature. Of the six caprine knees scanned, four had mean bone marrow signal intensities of 61±3 and two had mean bone marrow signal intensities of 282±6, and these values could be related to age. As shown in Figure 6, hypointense haemopoetic red bone marrow (B) in the immature caprine knees and hyperintense yellow marrow (C) in the older more skeletally mature caprine knees can be seen. Unfused epiphyseal plates (A) were noted in one of the caprine knees suggesting it was less than 3 months of age.

The outcomes of the angle sensitive MRI investigation were found to be strongly related to maturity. Figure 7 shows typical results of the patella tendon for an immature sample (A,C,E), estimated to be <3 months of age and a mature sample

(B,D,F) estimated to be >3 years of age, with the plots of raw 3D vector field data, 3D tractography plots and orientation distribution plots. The alignment index corresponding to the dominant direction was calculated in each case.

It can be clearly seen that the immature specimen has very much less aligned collagen fibre tracts whereas the skeletally mature specimen is highly aligned. This is reflected in the distribution plots and in the calculated alignment indices, where the immature caprine (Figure 7A) had AI = 0.46 while the mature (Figure 7B) caprine had AI = 0.97.

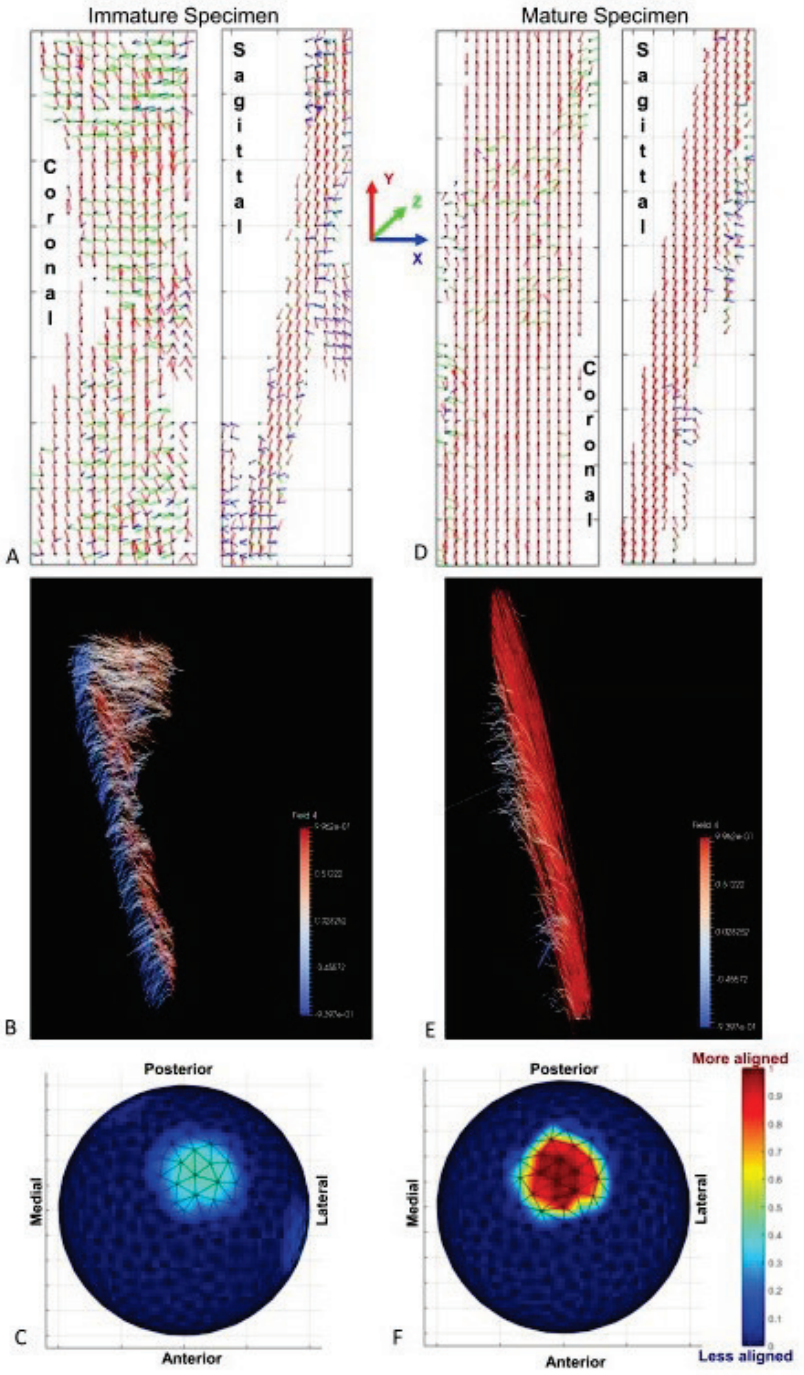

FIGURE 7 Representative results obtained for an immature (A,B,C) patella tendon, estimated <3 months, and a mature (D,E,F) estimated >3 years. 3D vector field plots show the computed collagen orientations in the sagittal and the coronal plane for an immature (A), and a mature specimen (D), with the directions coded in colour for easier visualisation. The corresponding 3D tractography plot for the immature specimen (B) shows a significantly less aligned collagen fibre structure than for the mature specimen (E). Orientation distribution plot for the immature specimen (C) also shows a significantly less pronounced peak with a calculated AI=0.46, compared to the mature specimen (F) with AI=0.97.

The results for all nine caprine samples are summarised in Figure 8, showing the fibre distribution plots for all 6 caprine knees, ordered according to their increasing estimated age, with the calculated AI values for the patella tendon in each case. A high level of correspondence can be observed between the estimated age, AI value and orientation distribution plots.

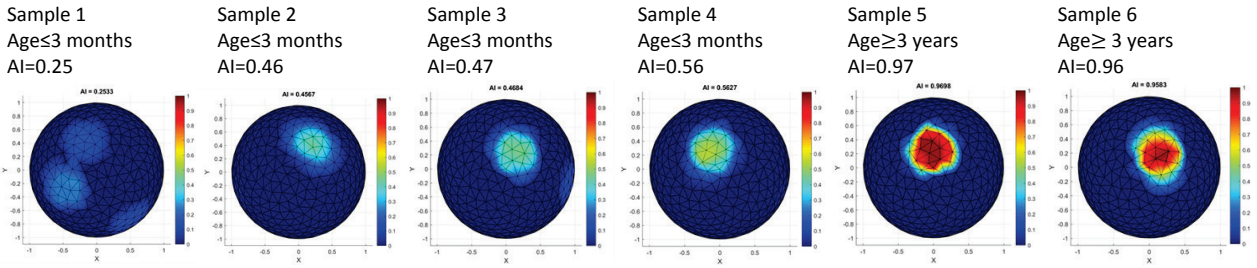

FIGURE 8 Fibre alignment distribution plots for the caprine knee samples 1-6 with calculated and Alignment Indices (AI) and estimated ages. The least aligned patella tendon was from knee 1 which was the least mature (≤3 months, AI=0.25), samples 2 – 4 are more mature (≤6 months, AI range 0.46 – 0.56), while samples 5 and 6 are very mature (≥36 months, AI of 0.96 and 0.97).

3.2.2 Canine Knee Samples

Dogs have a cranial caudal ligament (CCL) which is similar to the anterior cruciate ligament (ACL) in humans. It is composed of two bundles, an anteromedial (AM) bundle and a posterolateral (PL) bundle. Two canine knees were found to be damaged with partial CCL tears, where the PL bundle was intact but the AM bundle was torn (Figure 9).

The fibre tracts are seen to be continuous in the healthy canine knee with no disruption of the ligament. For the partially torn CCL, the AM bundle fibres (red) are discontinuous and the PL bundle fibres (blue, behind) are continuous.

The differences in orientation distribution in Figure 9 can be clearly seen between a healthy and a damaged CCL. The damaged AM fibre bundle is evidently more diffuse compared to the undamaged AM. The undamaged PL fibre bundles in both cases show similar level of alignment as the undamaged AM.

The alignment indices may be calculated independently for the AM and PL fibre bundles. Table 1 summarises the results for all 10 specimens, noting that one specimen was found to be putrefied and unsuitable for analysis, while 3 of the samples were from very small dogs and the ligaments were too small for the resolution of 1mm used in this study. For the samples 1 and 2 where AM injury was detected, the corresponding AI values can be seen to be markedly reduced compared to those for the PL and to all AI values in the healthy specimens 3–5.

TABLE 1: Summary results of the canine CCL study showing calculated alignment indices and whether injury was detected on PM. Two alignment indices were calculated, corresponding to the anteromedial (AM) and posterolateral (PL) fibre bundles.

Sample #	Injury detected	Alignment index	
		AM	PL
1	Yes, AM	0.06	0.17
2	Yes, AM	0.08	0.19
3	No	0.25	0.18
4	No	0.22	0.21
5	No	0.26	0.25
6	No	0.22	0.17
7	Specimen putrefied	-	-
8, 9, 10	Specimen too small	-	-

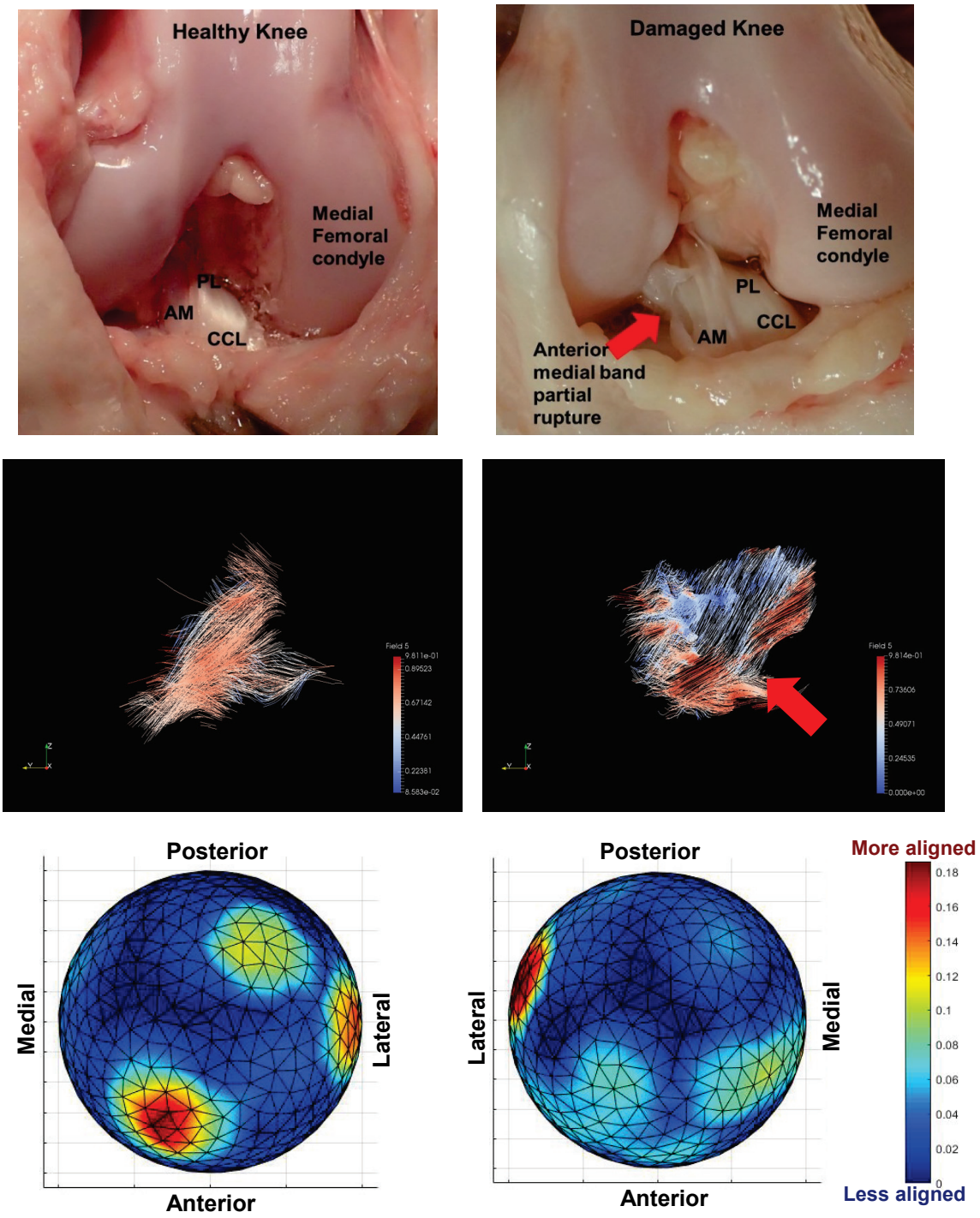

FIGURE 9 Dissection photographs of the knee joints from two canine specimens with corresponding tractography plots and fibre orientation distribution. LEFT: Healthy left knee where the photographed CCL is shiny and bright. RIGHT: Damaged right knee with a partial tear of the CCL involving the anteromedial bundle (AM), while the posterolateral bundle (PL) is still intact. Note that for the partially torn AM ligament the photograph shows that the shininess of the ligament has disappeared, the tractography plot shows discontinuous fibres of the AM band, and the orientation distribution plot shows a significant reduction of alignment.

4. DISCUSSION

The studies have shown that the proposed Magic Angle Directional Imaging method achieves high robustness and high accuracy with a much smaller set of orientations of the subject relative to B_0 than reported previously. This is primarily the result of selecting equispaced scanning direction, which are better at capturing the shape of the 3D characteristic of signal intensity I with angle θ, then the previously suggested directions confined in 2 or 3 planes. Bearing in mind that no *a priori* knowledge about approximate fibre directions has been assumed, in the future it would be interesting to assess what further reductions in the number of sample orientations could be achieved by utilising such a priori knowledge. The accuracy of orienting the subject w.r.t. B_0 is not important and orientations within a few degrees from the nominal were found to be perfectly adequate, as they still capture the underlying variation sufficiently well.

The accuracy of registration, however, is highly important for two reasons. First, it is necessary to accurately establish voxel correspondences so that the angle dependent intensity variation is accurately captured. Second, the rotation values of the registration are used in the calculation of the initial guess for fibre orientation estimation. In this work the rigid body registration based on fiducial markers provided sufficiently accurate alignment in rotation, but interactive adjustment of translation alignment was found to be necessary in order to achieve accurate voxel correspondences in the region of interest, though translation only involved distances of about one voxel. The main source of registration errors was found to be the presence of geometric distortions of MR images due to gradient non-linearity and any field inhomogeneity, with the distortion of the imaged subject being different in different acquired views. In our experiments the samples were centred at the scanner isocentre where the distortions would be minimal, but that meant that the passive markers, on which the registration is based, ended up several centimetres away from the isocentre where the geometric distortion becomes noticeable in the images of about 1mm resolution. In this work, geometric correction was applied to all images using the standard scanner functionality, but the correction was found to be imperfect and the residual geometric errors were still noticeable. Those errors could be further reduced through an additional, more accurate, calibration of the scanner. In this work, the additional manual fine alignment was employed and produced satisfactory results, but a more elegant solution would be to adopt soft registration such as that in [20]. Soft registration was not employed in this study because of the potential uncertainties and complexity in setting appropriate deformation parameters, though it will be investigated in future work.

The robustness of overall method was for estimating fibre directions was found to be high, though it clearly depends on the image SNR value. Our aim was to achieve 99% success rate in calculating fibre orientations, but if this target is slightly lowered, then using fewer scanning directions may still be acceptable. For example the results for $SNR = 20$ and $N = 7$ scanning direction are sufficient to achieve 99.88% success rate, while $N = 5$ gives 98.5% success rate. In the case of very low SNR=10, choosing $N = 9$ will still result in 99.88% success rate. This has implications for future applicability of the method, where significant savings in scanning time can be achieved by trading image SNR to produce useful results.

The accuracy and speed of the simplex minimisation in finding the fibre orientations represent several-fold improvements over previous methods. With SNR=20, errors $< 0.5°$ can be achieved, while SNR=10 gives error of about 1°. This is encouraging, as the experience gained through experiments has shown that achieving high accuracy is important because it leads to a more accurate orientation distribution analysis and consequently better differentiation between different cases.

Regarding caprine specimens, the expected outcome of highly aligned patella tendons was only demonstrated in skeletally mature samples. It was initially understood from the meat supplier that the caprine specimens would be aged around 12 months (±6months), but in fact the six caprine knees studied were found to range in age from less than 3 months to more than 3 years. The very immature specimens were identified by the femoral and tibial growth plates, red bone

marrow, while the mature ones were identified by skeletal maturity and yellow bone marrow. Image hypointensity was demonstrated by red marrow that contains approximately 40% fat, 40% water and 20% protein [21]. Image hyperintensity was seen with yellow marrow that contains approximately 80% fat, 15% water and 5% protein. The findings of the imaging study were found to correlate well with the known changes in collagen structure in tendons with age. The mean collagen fibril length is known to increases from birth to maturity [22] and the fibrils in mature ligaments and tendons are known to be either continuous or functionally continuous [23].

Regarding canine specimens, CCL disease is a known gradual degeneration of the ligament extracellular matrix (ECM) leading to ligament rupture [24]. Certain breeds of dog (e.g. Labrador Retreiver, Rottweiler, Newfoundland, Boxers) are at increased risk of developing CCL disease [25]. In the samples studied, the AM bundles were seen to be slightly more aligned than the PL bundles. This might be due to the position they were scanned in as the tension in the bundle will depend on the position of the femur and tibia i.e. flexion and extension. When the AM bundle is torn and smeared then the corresponding AI value was found to be less than half that of the PL bundle.

Partial ACL tears are extremely difficult to diagnose using traditional MR imaging which provides no functional assessment of the remaining portion [26]. However, using our magic angle imaging technique the partial ligament rupture may be clearly visualised. Based on the cases considered in this work, the AI can be concluded to provide a quantified measure of the alignment of the collagen fibre bundles and a potential basis for diagnostic assessment.

It remains very challenging to apply the proposed methods in *in vivo* imaging of human knees using conventional scanners. Reorienting the subject relative to the main field is nearly impossible in the closed bored scanners, where the field (z-axis) is the axis of the bore. In conventional open scanners, where the field is perpendicular to the poles, it is possible to rotate the magnet about one axis to rotate the field, but rotation about the second axis is restricted by the patient, and magnet rotation about the z-axis will not change the direction of the field. For these reasons we have proposed a new type of open MRI magnet [12] where the field is parallel to the poles and it can be rotated about two axes while the subject remains stationary.

A limitation of the proposed method is that it assumes a single dominant fibre direction in a voxel, and it calculates only one direction vector for each segmented voxel. It might be possible to deduce that some voxels contain crossing fibres by analysing their surrounding vector field as part of calculating the streamlines for the tractography plots, however this was outside the scope of our work.

A limitation of this study is that the fibre tracking method was not assessed against direct fibre imaging methods such as Polarised Light Microscopy, as such equipment was not available at the time of the study, and in the future it would be important to perform such assessment. Previously reported such studies [11] indicate that the accuracy of fibre estimation based on theoretical predictions using Equation (1) is high, though our estimation method is different and we expect a higher accuracy.

It was also not possible to carry out ultrashort echo time (UTE) imaging with the scanner that was available for this work, which may serve as a reference for detection of ligament injury [27]. In the future we intend to carry out such studies, and to investigate the value of the proposed method particularly in relation to quantitative MRI techniques such as UTE-T_2^* mapping.

The proposed Magic Angle Directional Imaging represents an alternative method to the Diffusion Tensor Imaging (DTI) [28-30], which is a widely used technique for fibre tractography. The present study did not involve a direct comparison with DTI though it would be useful to perform such investigation in the future. DTI is generally challenging for imaging of ligaments and tendons because of their very short T_2 (1–2 ms) compared to the long TE (50–90 ms) typically required for the diffusion encoding gradients, with a resulting low signal. This requires the subject to be positioned at or near the magic

angle in order to increase T_2 sufficiently, while TE also needs to be reduced by employing suitably modified imaging sequences, such as that in [30]. The recent DTI study in [29] involved of ACL graft, where the specific tissue properties allowed the use of relatively long TE=45ms

The recently reported use of Susceptibility Tensor Imaging (STI) [31] also represents a potential alternative method, which is based on the susceptibility anisotropy of collagen and involves obtaining phase images at 12–15 different orientations relative to B_0. STI in this context has so far been demonstrated only at very high fields and demands a similar imaging procedure to the one that exploits the magic angle effect.

Our future work will be directed towards obtaining equivalent MR imaging results in-vivo. This necessitates the use of new MRI scanner types such as the transverse field open magnet currently under development in our labs [12]. As this is a low field machine, it faces the challenge of achieving images with a sufficiently high SNR. However, the simulation studies conducted so far indicate that even for low SNR values it would be sufficient to employ only 9 scanning directions, to achieve success rate of around 99% in estimating fibre directions, with the estimation accuracy of the order of 1.5°. These results are highly encouraging, though clearly further such assessment is needed in relation experimentally obtained *in vivo* images.

5. CONCLUSIONS

Our results indicate that Magic Angle Directional Imaging can detect injury such as partial ligament tears, and it can be used to visualise maturity related changes in the collagen structure of tendons. To our knowledge this is the first study to show such results, suggesting that the method can serve as the basis for a future non-invasive diagnostic tool. The proposed method employs a significantly smaller number of scanning directions than in previous work, while the minimum number of scans is largely determined by the image noise. Monte Carlo simulation studies indicate that the method for estimating fibre orientations is robust and accurate in the presence of noise. The Alignment Index was found to be a useful measure for quantitative assessment of fibre structure anisotropy, which may be useful in the future to establish diagnostic criteria and to augment the visual analysis of 3D tractography data. Application of the method to human imaging will demand the use of new magnet configurations, such as that proposed in [12], which are able to provide less restricted control of the field orientation to the subject than the conventional closed bore, or the conventional open MRI scanners.

ACKNOWLEDGEMENTS

This work was supported by the National Institute for Health Research (NIHR) Invention for Innovation (i4i) under Grant II-LA-1111-20005. We are grateful to Charing Cross Hospital MRI department and Imaging Committee for the kind use of the Siemens 3T Verio. We would also like to thank the RVC PM technician Richard Prior for his assistance with canine knee collection.

ORCID: Mihailo Ristic http://orcid.org/0000-0003-4837-9518

REFERENCES

1. Amin NH, Hussain W, Ryan J, Morrison S, Miniaci A, Jones MH. Changes Within Clinical Practice After a Randomized Controlled Trial of Knee Arthroscopy for Osteoarthritis. *Orthopaedic Journal of Sports Medicine.* 2017;5(4):2325967117698439.

2. Devitt BM, O'Sullivan R, Feller JA, et al. MRI is not reliable in diagnosing of concomitant anterolateral ligament and anterior cruciate ligament injuries of the knee. *Knee Surgery, Sports Traumatology, Arthroscopy.* 2017;25(4):1345-1351.
3. Hamilton DF, Howie CR. Knee arthroscopy: influence of systems for delivering healthcare on procedure rates. *BMJ: British Medical Journal.* 2015;351.
4. Berendsen HJ. Nuclear magnetic resonance study of collagen hydration. *The Journal of Chemical Physics.* 1962;36(12):3297-3305.
5. Fullerton G, Cameron I, Ord V. Orientation of tendons in the magnetic field and its effect on T2 relaxation times. *Radiology.* 1985;155(2):433-435.
6. Erickson S, Cox I, Hyde J, Carrera G, Strandt J, Estkowski L. Effect of tendon orientation on MR imaging signal intensity: a manifestation of the" magic angle" phenomenon. *Radiology.* 1991;181(2):389-392.
7. Bydder M, Rahal A, Fullerton GD, Bydder GM. The magic angle effect: a source of artifact, determinant of image contrast, and technique for imaging. *Journal of Magnetic Resonance Imaging.* 2007;25(2):290-300.
8. Henkelman RM, Stanisz GJ, Kim JK, Bronskill MJ. Anisotropy of NMR properties of tissues. *Magnetic Resonance in Medicine.* 1994;32(5):592-601.
9. Szeverenyi NM, Bydder GM. Dipolar anisotropy fiber imaging in a goat knee meniscus. *Magnetic resonance in medicine.* 2011;65(2):463-470.
10. Krasnosselskaia LV, Fullerton GD, Dodd SJ, Cameron IL. Water in tendon: orientational analysis of the free induction decay. *Magnetic Resonance in Medicine.* 2005;54(2):280-288.
11. Seidel T, Hammer N, Garnov N, Schneider G, Steinke H. An algorithm for the calculation of three-dimensional collagen fiber orientation in ligaments using angle-sensitive MRI. *Magnetic Resonance in Medicine.* 2013;69(6):1594-1602.
12. McGinley JV, Ristic M, Young IR. A permanent MRI magnet for magic angle imaging having its field parallel to the poles. *Journal of Magnetic Resonance.* 2016;271:60-67.
13. de Oliveira A, Rauschenberg J, Beyersdorff D, Semmler W, Bock M. Automatic passive tracking of an endorectal prostate biopsy device using phase-only cross-correlation. *Magnetic Resonance in Medicine.* 2008;59(5):1043-1050.
14. Parker JR. *Algorithms for image processing and computer vision.* John Wiley & Sons; 2010.
15. Franco E, Brujic D, Rea M, Gedroyc WM, Ristic M. Needle-guiding robot for laser ablation of liver tumors under MRI guidance. *IEEE/ASME Transactions on Mechatronics.* 2016;21(2):931-944.
16. Galassi F, Brujic D, Rea M, Lambert N, Desouza N, Ristic M. Fast and accurate localization of multiple RF markers for tracking in MRI-guided interventions. *Magnetic Resonance Materials in Physics, Biology and Medicine.* 2015;28(1):33-48.
17. Arun KS, Huang TS, Blostein SD, Intelligence M. Least-squares fitting of two 3-D point sets. *IEEE Transactions on Pattern Analysis.* 1987(5):698-700.
18. Lagarias JC, Reeds JA, Wright MH, Wright PE. Convergence properties of the Nelder--Mead simplex method in low dimensions. *SIAM Journal on optimization.* 1998;9(1):112-147.
19. Leopardi P. A partition of the unit sphere into regions of equal area and small diameter. *Electronic Transactions on Numerical Analysis.* 2006;25(12):309-327.
20. Klein S, Staring M, Murphy K, Viergever MA, Pluim JP. Elastix: a toolbox for intensity-based medical image registration. *IEEE transactions on medical imaging.* 2010;29(1):196-205.
21. Małkiewicz A, Dziedzic M. Bone marrow reconversion–imaging of physiological changes in bone marrow. *Polish journal of radiology.* 2012;77(4):45.
22. Craig AS, Birtles MJ, Conway JF, Parry DA. An estimate of the mean length of collagen fibrils in rat tail-tendon as a function of age. *J Connective tissue research.* 1989;19(1):51-62.
23. Provenzano PP, Vanderby Jr R. Collagen fibril morphology and organization: implications for force transmission in ligament and tendon. *Matrix Biology.* 2006;25(2):71-84.
24. Comerford E, Smith K, Hayashi K. Update on the aetiopathogenesis of canine cranial cruciate ligament disease. *Veterinary Comparative Orthopaedics Traumatology.* 2011;24(02):91-98.
25. Taylor-Brown FE, Meeson RL, Brodbelt DC, et al. Epidemiology of cranial cruciate ligament disease diagnosis in dogs attending primary-care veterinary practices in England. *Veterinary Surgery.* 2015;44(6):777-783.
26. Temponi EF, de Carvalho Júnior LH, Sonnery-Cottet B, Chambat P. Partial tearing of the anterior cruciate ligament: diagnosis and treatment. *Revista Brasileira de Ortopedia.* 2015;50(1):9-15.
27. Chang EY, Du J, Chung CB. UTE imaging in the musculoskeletal system. *Journal of magnetic resonance imaging.* 2015;41(4):870-883.
28. Ferizi U, Rossi I, Lee Y, et al. Diffusion tensor imaging of articular cartilage at 3T correlates with histology and biomechanics in a mechanical injury model. *Magnetic Resonance in Medicine.* 2017;78(1):69-78.
29. Van Dyck P, Froeling M, De Smet E, et al. Diffusion tensor imaging of the anterior cruciate ligament graft. *Journal of Magnetic Resonance Imaging.* 2017;46(5):1423-1432.
30. Wengler K, Tank D, Fukuda T, et al. Diffusion tensor imaging of human Achilles tendon by stimulated echo readout-segmented EPI (ste-RS-EPI). *Magnetic resonance in medicine.* 2018;80(6):2464-2474.

31. Wei H, Gibbs E, Zhao P, et al. Susceptibility tensor imaging and tractography of collagen fibrils in the articular cartilage. *Magnetic Resonance in Medicine.* 2017;78(5):1683-1690.

List of figures and tables with captions

FIGURE 1 Data processing steps following registration of image volumes acquired at different orientations to the field B_0. **A**: Region of interest is interactively selected, voxels within it with intensity variations exceeding a threshold are highlighted as white, and segmented. **B**: Dominant fibre orientations in each voxel are determined and displayed as a 3D vector field. **C**: 3D polar plot of the frequency distribution of fibre orientations in the segmented voxels.

FIGURE 2 9 equidistant orientation vectors relative to B_0 in which the samples were scanned: (0, 0, 1), (0.661, 0, 0.75), (0, 0.661, 0.75), (-0.661, 0, 0.75), (0, -0.661, 0.75), (0.65, 0.65, 0.4), (-0.65, 0.65, 0.4), (-0.65, -0.65, 0.4), (0.65, -0.65, 0.4).

FIGURE 3 **A:** Goat knee after it had been cut down to 175mm and thoroughly cleaned of metal debris. **B**: Knee wrapped in polythene to prevent leakages and maintain tissue hydration covered in clear parcel tape to immobilise knee in extension. **C:** Goat knee within the test sphere with the proximal and distal ends embedded in white Plasticine. **D**: Test sphere containing goat knee within the 12 channel head coil in specially designed holder ready to begin scanning in position 1.

FIGURE 4 Monte Carlo simulation results showing number of failed (error> 5°) fibre orientation calculations in 10^5 simulations as a function of image SNR, for different numbers of equidistant scanning orientations relative to B_0.

FIGURE 5 Average and standard deviation of error in estimating fibre directions as a function of SNR, using 250 test directions to find the initial guess for simplex minimisation. Each point involves 10^3 Monte Carlo simulations.

FIGURE 6 3D T1 FLASH central slice from three of the six specimens scanned showing the variation in the signal intensity of the immature (**A** and **B)** and mature (**C**) bone marrow. The femoral and tibial epiphyseal growth plates are unfused in the very immature (**A**) specimen which also has a similar signal intensity to the immature (**B**) specimens.

FIGURE 7 Representative results obtained for an immature (A,B,C) patella tendon, estimated <3 months, and a mature (D,E,F) estimated >3 years. 3D vector field plots show the computed collagen orientations in the sagittal and the coronal plane for an immature (A), and a mature specimen (D), with the directions coded in colour for easier visualisation. The corresponding 3D tractography plot for the immature specimen (B) shows a significantly less aligned collagen fibre structure than for the mature specimen (E). Orientation distribution plot for the immature specimen (C) also shows a significantly less pronounced peak with a calculated AI=0.46, compared to the mature specimen (F) with AI=0.97.

FIGURE 8 Fibre alignment distribution plots for the caprine knee samples 1-6 with calculated and Alignment Indices (AI) and estimated ages. The least aligned patella tendon was from knee 1 which was the least mature (≤3 months, AI=0.25), samples 2 – 4 are more mature (≤6 months, AI range 0.46 – 0.56), while samples 5 and 6 are very mature (≥36 months, AI of 0.96 and 0.97).

FIGURE 9 Dissection photographs of the knee joints from two canine specimens with corresponding tractography plots and fibre orientation distribution. LEFT: Healthy left knee where the photographed CCL is shiny and bright. RIGHT: Damaged right knee with a partial tear of the CCL involving the anteromedial bundle (AM), while the posterolateral bundle (PL) is still intact. Note that for the partially torn AM ligament the photograph shows that the shininess of the ligament has disappeared, the tractography plot shows discontinuous fibres of the AM band, and the orientation distribution plot shows a significant reduction of alignment.

TABLE 1: Summary results of the canine CCL study showing calculated alignment indices and whether injury was detected on PM. Two alignment indices were calculated, corresponding to the anteromedial (AM) and posterolateral (PL) fibre bundles